The Electrochemistry of Iron Oxide Thin Films Nanostructured by High Ion Flux Plasma Exposure

Rochan Sinha[a,*], İrem Tanyeli[a,1], Reinoud Lavrijsen[b], M. C. M. van de Sanden[a,b], Anja Bieberle-Hütter[a]

[a]Dutch Institute for Fundamental Energy Research (DIFFER), P.O. Box 6336, 5600 HH Eindhoven, The Netherlands

[b]Department of Applied Physics, Eindhoven University of Technology (TU/e), P.O. box 513, 5600 MB Eindhoven, the Netherlands

*Corresponding author email address: r.sinha@differ.nl

Abstract

Photo-electrochemical (PEC) water splitting of hematite photoanodes suffers from low performance and efficiency. One way to increase the performance is to increase the electrochemically active surface area available for the oxygen evolution reaction. In this study, we use high ion flux, low energy helium plasma exposure to nanostructure sputtered iron thin films. Subsequent annealing in air at 645°C leads to the formation of PEC active hematite (α-Fe$_2$O$_3$) phase in these films. The surface area, as derived from electrochemical impedance spectroscopy (EIS), was seen to increase 10-40 times with plasma exposure. The photocurrent density increased by 2-5 times for the plasma exposed films as compared to the unexposed films. However, the less nanostructured film showed a higher photocurrent density. These findings were explained by detailed chemical and structural characterization in combination with electrochemical characterization and attributed to the presence of secondary elements in the film as well as to the presence of secondary iron oxide phases apart from hematite. This work demonstrates the complex effect of plasma exposure on both film morphology and chemical composition of PEC thin films and provides further understanding on how this technique can be used for nanostructuring of other functional films.

[1]Current address: Department of Applied Physics, Chalmers University of Technology, 412 96 Göteborg, Sweden

1. Introduction

Solar energy has emerged as an excellent alternative energy source to fossil fuels due to its abundance, renewability and low environmental impact. However, the intermittent nature of solar energy as well as regional and seasonal variations entail the need for an efficient, large-scale storage solution. One strategy would be to convert the solar energy into chemical fuels, known as 'solar fuels'. A widely researched technique for generation of solar fuels is photo-electrochemical (PEC) water splitting [1, 2]. In this process, hydrogen (H_2) and oxygen (O_2) are generated from water utilising solar energy as a driving force.

However, in order to be competitive with other hydrogen generation techniques such as steam reforming or electrolysis of water, the efficiency of the water splitting process has to be improved. A significant bottleneck is the availability of suitable materials for water splitting. An ideal single photo-electrode material should have a band gap which straddles both the hydrogen and oxygen redox potentials to provide sufficient energy to drive the PEC water splitting reaction. It should demonstrate suitable electronic and catalytic properties to drive the water splitting reactions. It would also need to be earth-abundant and stable under harsh PEC water splitting conditions. Metal oxide-based materials are promising mainly due their stability, however, up to now, no single material has been proven to meet all these conditions. An alternative to this single photo-electrode material approach is a tandem configuration combining a large band gap n-type material for the oxygen evolution reaction (OER) and a narrower band gap p-type material for the hydrogen evolution reaction (HER). This allows for using specific materials for the OER and the HER half-reactions [2-6].

Hematite (α-Fe_2O_3) is a promising material for the OER half-reaction due to an optimum bandgap (2-2.2 eV), excellent chemical stability, non-toxicity, abundance and low cost [7-11]. The bandgap of hematite allows a theoretical solar-to-hydrogen efficiency of approximately 12-16% [12]. However, the highest experimentally reported value so far was 3.1% [13]. This large disparity is related to the poor light absorptivity due to an indirect bandgap transition and to a short minority carrier lifetime (~10 ps) and low mobility (0.2 cm^2 V^{-1} s^{-1}) [8, 14]. The former requires a relatively thick film (400-500 nm) for complete light absorption [15] while the latter requires films with a thickness lower than 50 nm to account for the extremely short hole diffusion length of 2-4 nm [16]. Nanostructuring of hematite permits the creation of thin films with a large surface area for sufficient light absorption, along with low thickness to improve charge collection efficiency. A larger surface area also allows for a greater number of sites at which the oxygen evolution reaction can occur. These factors lead to improvement in its water-splitting performance. Various nanostructures have been developed such as nanowires, nano-corals, dendritic structures and leaflet-type structures in order to improve the PEC performance of hematite [17-21]. However, control over the morphology of the obtained nanostructure remains a major challenge.

Low energy helium-ion plasma exposure has been demonstrated to provide controlled growth of nanostructures on the surface of bulk iron films by varying plasma exposure time and surface temperature [22]. Controlled nanostructure growth via plasma exposure led to a five-fold improvement in photocurrent density over dense, non-nanostructured bulk tungsten trioxide (WO_3) [23]. Bieberle et al. showed successfully that iron thin films can be nanostructured by high flux, low energy helium plasma [24]. Stable and well-adhering films were fabricated on FTO-coated glass. In this work, structural and chemical characterization of such plasma nanostructured thin films by techniques such as SEM, XRD, XPS and Raman spectroscopy are related to the photoelectrochemical properties measured by

chronoamperometry, cyclic voltammetry and electrochemical impedance spectroscopy in order to elucidate the mechanisms by which plasma exposure effects the water splitting performance of these thin films.

2. Experimental methods

All films were deposited by DC magnetron sputtering on glass substrates (1 mm thick) with F: SnO2 (FTO) conducting layer of approximately 450 nm (Solaronix S. A.). A sputter tool from Kurt J. Lesker was used with a base pressure $<10^{-8}$ mbar and a target-substrate distance of 95 mm. All depositions were carried out at room temperature with an Ar pressure of 1 Pa and a power of 100 W using a 2" Fe sputter target. The films were sputtered for 881 s to obtain a film thickness of 200 nm ± 10 nm. High-ion flux low energy helium plasma exposure was carried out in the Pilot PSI set-up at DIFFER [25]. The films were exposed to a low energy helium plasma (20 eV) with an ion flux of $1-1.4 \times 10^{23}$ m^{-2} s^{-1} at a surface temperature of 650°C. The base pressure was maintained in the range 10^{-4}-10^{-5} mbar. For the short plasma exposed (SE) film, plasma exposure duration was 20 min and for the long plasma-exposed (LE) film, the duration was 50 min. Plasma-exposed thin films, along with an unexposed film (UE) were annealed in air at a temperature of 645°C for 10 min. A ramp rate of 5°C min^{-1} was applied to reach the desired annealing temperature.

The morphologies of the thin films were examined by a field emission scanning electron microscope (SEM) (Zeiss Sigma) with an in-lens detector and 5 kV accelerating voltage. Structural characterization was performed using a Bruker D8 Eco X-ray diffractometer (XRD) with a Cu Kα (λ= 1.5406 Å) source and a Lynx-eye detector in a grazing incidence configuration at an incident angle of 3° and in the 2θ range from 20° to 80°. A Renishaw Invia spectrometer was utilised for Raman analysis using an excitation wavelength of 514 nm. A Thermo Scientific K-Alpha X-ray photoelectron spectroscopy (XPS) setup equipped

with an Al Kα source (hν = 1486.6 eV) was used for the chemical analysis. Binding energy was corrected with respect to the C 1s peak at 284.5 eV. Optical absorbance of the films were characterized with a Perkin Elmer 1050 UV/Vis/NIR spectrophotometer in the wavelength range of 300 nm to 950 nm.

An in-house three-electrode electrochemical cell fitted with a quartz window was used for photoelectrochemical characterization. An aqueous solution of 1M NaOH (pH 13.6) was used as the electrolyte. A coiled Pt wire and an Ag/AgCl/Sat. KCl electrode (XR 300, Radiometer Analytical) were used as the counter electrode and reference electrode, respectively. The geometric area of the working electrode exposed to the electrolyte was 0.785 cm^2. The potential of the electrode was controlled with a BioLogic SP-150 potentiostat. All potentials reported are versus RHE through the relation [2]-

$$\Phi_{RHE} = \Phi_{Ag/AgCl} + \Phi^o_{Ag/AgCl\ vs\ RHE} + 0.059 \times pH \qquad (1)$$

With $\Phi^o_{Ag/AgCl\ vs\ RHE}$ = 0.197 V versus RHE at 25°C. Illumination was provided by an AM 1.5 class A solar simulator (LCS 100, Oriel Instruments) using a 100 W Xe lamp with a calibrated illumination intensity of 80 mW cm^{-2} at the sample position. All measurements were done at potentials between 0.6 V and 1.6 V versus RHE. Cyclic voltammetry measurements were performed at a scan rate of 20 mV s^{-1}. The onset potential was taken as the potential at which the first derivative of the photocurrent density with respect to the potential (dj/dV) achieved four times the value observed for the first derivative of the dark current measurement. This technique was adopted from [14]. Transient photocurrent measurements were obtained by chopping the incident light with an externally controlled shutter at a rate of 0.5 s^{-1} while performing linear sweep voltammetry (LSV) at a scan rate of 10 mV s^{-1}. Light chopping at a rate of 0.033 s^{-1} was utilised for chronoamperometry measurements at fixed potential values of 1.3 V and 1.5 V versus RHE. Electrochemical

impedance spectroscopy (EIS) was performed in a frequency range of 0.1 Hz to 100 kHz (lowest frequency point for UE was 0.2 Hz). The magnitude of the modulation signal applied to the potential was 10 mV. The potential at which the EIS scans were performed was increased step-wise between 0.6 V and 1.6 V versus RHE. Equivalent circuit fitting of the EIS spectra was performed using the ZView® software.

3. Results and discussion

Figures 1 (a)-(c) are the top-view and (d)-(f) are the cross-sectional SEM images of the UE, SE and LE films after annealing and PEC measurements. The morphology remains stable after PEC measurement when compared to the morphology found for as-annealed films [24].

For the UE film, a relatively smooth film surface is observed from the top-view image (figure 1(a)), along with the presence of nanowires and shallow voids which are formed during thermal oxidation of iron [26-31]. From the cross-section image (figure 1(d)), the thickness of the film is found to be 433 nm ± 20 nm. The variation in film thickness is calculated from measurements at arbitrary points across the film cross-section. This is very close to the expected thickness of 428 nm for a hematite (α-Fe_2O_3) thin film starting from a pure Fe layer of 200 nm thickness and assuming zero porosity. The calculation of the expected thickness is given in the supporting information. The observed thickness suggests that the UE film is very dense, with a porosity of less than 1%, as calculated from equation (2),

$$\text{Porosity (\%)} = 100 \text{ x} \left(1 - \frac{\text{Calculated Fe}_2\text{O}_3 \text{ thickness (from known Fe thickness)}}{\text{Actual Fe}_2\text{O}_3 \text{ film thickness (from cross-sec. SEM)}} \right) \quad (2)$$

The cross section image also shows that two morphologies are present in the iron oxide film after annealing, with smaller grains observed close to the FTO and large, elongated grains extending upwards from this bottom layer. This is attributed to the conversion of the dense iron layer (density = 7.26 g cm^{-3}) to a less dense iron oxide layer (density = 5.26 g cm^{-3}) [32].

The bottom layer has similar grain size as the initial iron layer, while the larger, elongated grains are formed on top due to the outward diffusion of iron atoms to the surface which reacts with the oxygen.

For the SE film, the top view SEM image (figure 1(b)) reveals a rough surface with small, globular clusters as well as pinholes and large cracks in the film. The cross-section SEM image (figure 1(e)) shows that the film has a thickness of 676 nm ± 60 nm, which is much higher than the expected thickness of 428 nm. This is due to plasma exposure process which leads to a highly porous film with a calculated porosity of 37% from equation (2). The high porosity occurs as a result of the diffusion and coalescence of helium ions into the iron thin film during plasma exposure [22, 23]. The larger variation in film thickness seen for the SE film is related to the Gaussian profile of the plasma plume as well as due to physical sputtering of the iron during the plasma exposure [24]. The cross-section of the SE film also shows two morphologies, with a dense upper layer with larger grains through which the helium ions diffuse inwards and create tiny pinholes and 'tunnels'. The helium coalesces to form larger pores in the lower region which consists of smaller grains, thus giving rise to larger porosity closer to the interface with the FTO.

The LE film, with a longer plasma duration has a very different morphology as compared to the other two films. From the top-view (figure 1(c)) and cross-section (figure 1(f)) SEM images, we can observe a highly porous film with nano-pillar like structure having a feature size of 50-200 nm and extending through the entire film thickness. This is due to the fact that a longer plasma duration leads to increased coalescence and subsequent 'bursting' of helium ions bubbles as well as diffusion of metal atoms due to the force of the high ion flux helium ions [22, 23]. The LE film has a thickness of 551 nm ± 135 nm. The larger variation in the film thickness is due to higher amount of physical sputtering of the iron during the longer plasma exposure as compared to the SE film. The porosity cannot be calculated from

equation (2), due to the large variation in film thickness of the iron layer during plasma exposure as explained above. However, visually it can be seen that the LE film has a porosity higher than for the SE film.

In figure 2(a), the current density is plotted as a function of applied potential under dark and illuminated conditions for all thin films. The SE film has a significant dark current which is related to the contact of the electrolyte with the underlying FTO due to the cracks in the film as observed in figure 1(b). This leads to increase in dark current due to higher conductivity of FTO as compared to hematite [14, 33]. The low dark current for the LE film proves that the nanostructured film has no cracks and open porosity down to the FTO and that the electrolyte is not in direct contact with the FTO.

The photocurrent density under illumination is comparable to other studies where rather thick (200-1000 nm) sputtered iron oxide films were used [34, 35]; higher photocurrent densities were only found for much thinner films (40-50 nm). This is due to the small diffusion length of the minority charge carriers in hematite which leads to higher bulk recombination in thick films. [8, 10, 36]. The onset potential (V_{onset}) is 0.92 V versus RHE for LE, 1.02 V versus RHE for UE and 1.06 V versus RHE for SE (from the technique explained in sec. 2). The photocurrent for all thin films has similar values up to an applied potential of approximately 1.3 V versus RHE. At potentials higher than 1.3 V versus RHE, the photocurrent for the SE film rises rapidly. At 1.5 V versus RHE, it is 2 times higher than the LE film and 4.5 times higher than the UE film. This is confirmed by chopped light chronoamperometric measurements at 1.3 V and 1.5 V versus RHE as shown in figure 2 (b) and (c), respectively.

A higher photocurrent for the SE thin film is counterintuitive, since the highest photocurrent is expected for the thin film with the largest surface area, which is in this case the LE thin film. In [23], indeed, the highest photocurrent was measured for the plasma-exposed WO_3

with the highest degree of nanostructuring. Therefore, the higher photocurrent for the SE thin film has a different origin.

The chopped light measurements as shown in figure 2(b) also provide information about the transient behaviour of the photocurrent for the thin films (also see figure S1 in the supplementary information). On illumination, anodic (positive) transients are observed which illustrates the competition between charge transfer of holes for OER and the recombination of holes with electrons. On turning the illumination off, cathodic (negative) transients are observed due to recombination of accumulated holes with the electrons from the external circuit. This transient then decays to the steady-state dark current [37].

In this study, all thin films show anodic and cathodic transients at 1.3 V versus RHE (figure 2(b)), which is related to fast electron-hole surface recombination rate and slow oxidation kinetics at lower potentials. However, as the potential is increased to 1.5 V versus RHE, the transient peaks become very small for the UE and LE thin films. This can be attributed to the utilisation of a high percentage of the holes reaching the surface for OER due to the high applied potential. For SE, however, large transient peaks are seen even at a high potential of 1.5 V versus RHE which suggests that the density of accumulated holes at the interface is higher for SE than for the other two films.

 In order to understand the reason why the less nanostructured SE film shows a higher photocurrent than the highly nanostructured LE film at potentials greater than 1.3 V versus RHE, the structure and chemical composition of the thin films were characterized in detail by XRD, Raman spectroscopy and XPS.

The XRD and Raman spectra for the thin films are shown in figure 3(a) and (b), respectively. From the XRD spectra, the peak positions for the UE thin film correspond to the hematite phase (α-Fe_2O_3) and FTO substrate and are comparable to the literature for sputtered and

annealed iron oxide thin films on FTO [34, 36]. For the plasma exposed thin films SE and LE, additional peaks are identified (denoted as * in figure 3(a)) and can be attributed to either maghemite (γ-Fe_2O_3) or magnetite (Fe_3O_4). However, due to similar crystal structure of these two phases (cubic inverse spinel), it is difficult to differentiate between these two oxide structures from XRD analysis [38].

Raman spectroscopy was used in order to unambiguously confirm which phases of iron oxide are present in the plasma-exposed thin films (figure 3(b)). All thin films show the characteristic hematite peaks [34, 36, 39-41]. For UE film, the peaks at 225 cm^{-1} and 500.4 cm^{-1} are assigned to the A_{1g} modes of hematite, while the peaks at 245.1 cm^{-1}, 292.2 cm^{-1}, 409.1 cm^{-1} and 610.8 cm^{-1} are assigned to the E_g modes of hematite. A broad peak at 1314.3 cm^{-1} is also seen and is assigned to two-magnon scattering [39].

For LE film, an extra peak at 658.74 cm^{-1} is observed in addition to the hematite peaks and is assigned to the A_{1g} mode of the magnetite phase [39]. Magnetite (Fe_3O_4) is expected to be present as inclusions at grain boundaries of hematite grains [42] and/or close to the interface with substrate [35]. Formation of non-stoichiometric iron oxide ($Fe_{3-x}O_4$) during plasma exposure was also found in bulk iron [22]. This influences the final stoichiometry of the films after thermal annealing and explains the presence of magnetite in the LE thin film.

For SE film, broad peaks are seen around 350 cm^{-1}, 500 cm^{-1}, 700 cm^{-1}, 1400 cm^{-1} and 1550 cm^{-1} apart from the peaks corresponding to hematite. These are assigned to the maghemite phase [39-41]. The broadness of the maghemite peaks as compared to peaks for the hematite phase, is directly related to the crystallinity of the thin films and suggests that SE has very small crystallites and/or a low degree of crystallinity [34].

XPS analysis was performed for further study of the chemical composition of the films. High resolution Fe 2p and O 1s spectra are shown in the supporting information for the thin films

(figure S2 (a) and (b), respectively). The Fe 2p spectra displays a peak binding energy of ~711.2 eV for the Fe $2p_{3/2}$ peak, with a corresponding satellite peak at ~719.2 eV for all films. The peak positions are similar to those reported in the literature for Fe_2O_3 and FeOOH [42-47]. The O 1s spectra of the films show two features: a peak at ~530.2 eV and another peak at ~532.1 eV. The former peak is attributed to hematite lattice oxygen [48] and the latter can be attributed to either oxygen vacancies ($V_O^{\bullet\bullet}$) [47] or hydroxyl (OH^-) species [42] at the surface, related to formation of FeOOH at the surface of these films.

XPS analysis also revealed that secondary elements were introduced into the plasma exposed thin films (table S1 in supporting information). Plasma exposed samples contain a significant amount of tin (Sn) at the surface, with the SE thin film showing 1.4-2.6% and LE thin film showing 2-5% Sn content at the surface. This is attributed to the diffusion of Sn from the FTO into the film during the thermal annealing process [49, 50]. However, Sn is not seen at the surface for the UE film. This is due to the fact that SE and LE films are exposed to high temperature both during plasma exposure and annealing while the UE thin film was subjected to high temperature only during annealing. This additional thermal treatment during plasma exposure causes a higher Sn diffusion from the FTO for the plasma exposed films as compared to the unexposed film.

In SE thin film, silicon (Si) is also found in the range of 7-11% depending on the location of the XPS measurement. This uneven distribution suggests that the Si is introduced during the plasma exposure and is related to the Gaussian nature of the plasma plume. The formation of maghemite (γ-Fe_2O_3) in this film is attributed to the Si content in the film. According to [40, 51, 52], Si can stabilise the γ-Fe_2O_3 phase even up to annealing temperatures of 700°C.

In the LE thin film, Zn is found with a surface concentration of 1.25-2%. Other secondary elements found as trace elements at the surface of the two films are listed in table S1. Apart

from Sn, which diffuse from the FTO substrate, the presence of all other secondary elements are attributed to variation in the environment of the plasma exposure chamber. The effect of the secondary oxide phases present in the plasma-exposed film on their optical properties is shown in figure S3 in the supporting information.

Electrochemical impedance spectroscopy (EIS) measurements were performed in order to relate the differences in the morphology and chemical composition of the films to the PEC activity. The impedance response for UE, SE and LE at an applied potential of 0.8 V versus RHE are shown in figure 4 (a). Two main features are seen in the data. At high frequency, a distinct semi-circular arc is observed for all three films. The relaxation frequency is between 400-4500 Hz which is characteristic for processes occurring in the bulk of the semiconductor [33, 53]. The low frequency response is different for the different films as well as the applied potential. Based on the relaxation frequency of these processes, they are attributed to the charge transport and/or diffusion processes occurring at the semiconductor-electrolyte interface [8, 33, 54].

For evaluation and quantification of the different features observed in the EIS spectra, the data is fitted to an equivalent circuit model (ECM). For depressed semi-circles, the capacitors are replaced by constant phase elements (CPE) in the ECM in order to account for non-uniform current distribution at the nanostructured electrode surface. The CPE values are converted to capacitance values using the formula proposed by Brug et al. [55].

The ECM model used in this work was proposed by Klahr et al. [53] for a hematite thin film and assumes that the OER occurs via surface states present at the hematite-electrolyte interface. Various theoretical and experimental studies have shown the existence of these surface states in hematite thin films, as summarised in [7], and have been directly observed by Zandi et al. using operando ATR-FTIR technique [56]. In our study, some modifications

of the Klahr model are required in order to account for the features seen in the EIS spectra of plasma-exposed thin films. The modified Klahr model is shown in Figure 4(b) and consists of two extra elements, A and B for LE and SE thin films, respectively.

The elements used in the ECM are described as follows. The series resistance, R_s, includes the contributions from FTO, ionic conductivity of the electrolyte and the external contacting. The bulk capacitance, C_{BULK}, represents the electrical double layer at the semiconductor-electrolyte interface. The trapping resistance, R_{TRAP}, accounts for the trapping/de-trapping of charge carriers at the surface states. The charge transfer process through surface states at the hematite-electrolyte interface is described by the parallel connection of R_{CT1} and C_{CT1}. R_{CT1} is the charge transfer resistance for the OER and C_{CT1} is related to the density of charge carriers trapped at the hematite surface states. The general model is used for fitting the EIS spectra for the UE thin film.

The LE thin film shows, in addition, a diffusive behaviour at lower frequencies in the EIS spectra due to its open and porous structure. A Warburg element, represented as element A in figure 3(b) accounts for this effect [57]. For the SE thin film, a second charge transfer process is observed at low frequencies and is modelled by the element B, which is a parallel connection of resistance, R_{CT2}, and capacitance, C_{CT2}. The conditions under which the extra elements A and B are used in the ECM are specified in figure 4(c).

The electrical double layer at the semiconductor-electrolyte interface is a close approximation of the electrochemically active surface area of the thin film exposed to the electrolyte. As explained above, the bulk capacitance (C_{BULK}) in the ECM represents the electrical double layer and is, therefore, used to quantify the surface area of the thin films as shown in Figure 5(a). The surface area of UE is similar to those reported for thick hematite films in the literature [34, 58]. The surface area for LE and SE thin films are 40 times and 10 times larger

than for UE, respectively, which is in agreement with the increase in nanostructuring and porosity of the films with increase in plasma duration, as shown in figure 1.

Figure 5(b) shows the OER charge transfer resistance values from the hematite surface states (R_{CT1}). It is seen that the R_{ct1} values for the plasma exposed films (SE and LE) are an order of magnitude lower than for the unexposed film (UE). The larger surface area, as seen from the C_{BULK} values in figure 5(a), and the reduced OER charge transfer resistance from the hematite surface states, as seen from the R_{CT1} values in figure 5(b), can explain the higher photocurrent at potentials above 1.2 V versus RHE observed for the plasma exposed films as compared to the unexposed film. This is attributed to the higher Sn content in the plasma exposed films, which can increase charge transfer efficiency via surface states in hematite films [59]. Another possible reason for the lower R_{CT1} values for SE and LE thin films can be the presence of Si and Zn, respectively, which are known to improve the electronic properties of hematite [34, 60].

In order to understand why the less nanostructured SE film has a higher photocurrent than the highly nanostructured LE film, we need to consider two things. The first is that the LE thin film contains a large amount of magnetite (fig 2(b)) which can act as a bulk recombination centre for charge carriers [34, 42] and, thereby, reduces the photocurrent of the LE thin film. The second is the occurrence of a secondary charge transfer process in the SE film, apart from the charge transfer from the hematite phase.

Figure 6(a) and (b) shows the fitting data for the two RC circuits corresponding to the two separate OER processes occurring in the SE thin film. The first RC circuit corresponds to the charge transfer through the hematite surface states represented by R_{CT1} and C_{CT1} (orange circles). The second RC circuit corresponds to the second charge transfer process represented by R_{CT2} and C_{CT2} (purple squares).

It is observed that both RC circuits behave similarly, with rise in capacitance correlated with a concomitant decrease in the charge transfer resistance. This correlation between R_{CT1} and C_{CT1} was shown to be related to the OER occurring through surface states in hematite thin films [53]. Since R_{CT2} and C_{CT2} exhibit a similar correlation, it is postulated that the second OER process in the SE film also takes place via surface states. It is also observed that C_{CT2} is 3-4 orders of magnitude higher than C_{CT1}. This means that the surface state density is much higher for the second OER process as compared to the surface state density for the OER through hematite phase. This also explains the higher transients seen for SE thin films, since the available surface states for hole capture is much higher as compared to the other thin films. In addition, the R_{CT2} values sharply decrease with the increase in applied potential. It has a value 100 times larger than the R_{CT1} values of the hematite phase at low potential values (< 1.2 V versus RHE) but drops rapidly and becomes lower than R_{CT1} above 1.4 V versus RHE. The differences in the resistance and capacitance values of the second OER process in the SE thin film shows that the chemical nature of the surface states is different for this process.

It is known from literature that maghemite (γ-Fe_2O_3) has a higher onset potential than hematite due to its more resistive nature [61-64] and that the OER through maghemite also occurs via surface states [58]. Thus, the second OER process, which becomes active only at higher potentials with a sharp decrease in resistance values is attributed to charge transfer through surface states in the maghemite phase, which is only present in the SE film. Thus, while at lower potentials (<1.3 V versus RHE) the charge transfer occurs only through the hematite phase, at higher potential the reduction in charge transfer resistance and the high surface state density of the maghemite phase leads to the presence of a parallel OER pathway for the SE thin film. This explains the rapid rise in photocurrent for SE above 1.3 V versus RHE as compared to LE and UE, as seen in figure 2(a).

4. Conclusion

The effect of high ion flux, low energy helium plasma exposure on the PEC water splitting performance of iron-oxide thin films was investigated. It was observed that the degree of nanostructuring increased with increase in the plasma duration with more open, porous structures obtained. Using electrochemical impedance spectroscopy and equivalent circuit fitting, we could quantify the increase in the electrochemically active surface area of the films by calculating the bulk capacitance of the films. It was seen that the active surface area of the short exposed thin film increased 10 times and of the long exposed thin film increased 40 times as compared to the unexposed film. The increase in surface area is in line with the porosity calculated from the SEM images which is less than 1% for the unexposed film, while it is larger than 40% for the short exposed film. The porosity of the long exposed film is higher, although it could not be quantified due to sputtering of the iron layer during plasma exposure.

However, the higher degree of nanostructuring of the plasma exposed films did not lead to a concomitant increase in photocurrent density compared to the unexposed film with only 2-5 times increase in photocurrent density observed. This was partly related to the presence of defects, such as inclusion of magnetite phase (Fe_3O_4), which acts as a bulk recombination centre. The PEC performance was also found ~~in part~~ to be influenced by secondary elements, such as Sn, Si and Zn, which come from the substrate material or from the plasma exposure process and improve the charge transfer efficiency and electronic conductivity of the hematite phase present in these films. The incorporation of these secondary elements during plasma exposure can be reduced by changes in the exposure chamber such as use of a larger enclosure and molybdenum-based mounting materials to reduce sputtering of elements from the walls or target mounting region, respectively. Another method would be the usage of a pre-exposure argon plasma discharge to remove secondary elements close to the mounting

region, as well as use of in-situ, real time Optical Emission Spectroscopy to observe presence of secondary elements in the plasma.

Furthermore, it was found that the short exposed film with the lower degree of nanostructuring had a higher PEC performance than the highly nanostructured, long exposed film. This was explained by the presence of maghemite (γ-Fe_2O_3) in the film, which acted as a second, parallel OER pathway at potentials higher than 1.3 V versus RHE.

Thus, using various electrochemical techniques, we were able to gain a deep insight into the relation between the physico-chemical properties and the obtained PEC performance of the plasma-exposed thin films. It was found that the presence of secondary elements and other iron oxide phases in the films have a significant effect on the water splitting performance next to the degree of nanostructuring. This underlines the complexity of the plasma exposure process for thin film nanostructuring and can be used as a guideline to ensure that films with a controlled morphology and chemical composition can be fabricated in the future.

Acknowledgement

References

[1] A. Fujishima, K. Honda, Electrochemical Photolysis of Water at a Semiconductor Electrode, Nature, 238 (1972) 37-38.

[2] R. Van de Krol, M. Grätzel, Photoelectrochemical hydrogen production, 1 ed., Springer, United States, 2012.

[3] M.G. Walter, E.L. Warren, J.R. McKone, S.W. Boettcher, Q. Mi, E.A. Santori, N.S. Lewis, Solar water splitting cells, Chem Rev, 110 (2010) 6446-6473.

[4] H.M. Chen, C.K. Chen, R.-S. Liu, L. Zhang, J. Zhang, D.P. Wilkinson, Nano-architecture and material designs for water splitting photoelectrodes, Chemical Society Reviews, 41 (2012) 5654-5671.

[5] K. Rajeshwar, A. Thomas, C. Janáky, Photocatalytic Activity of Inorganic Semiconductor Surfaces: Myths, Hype, and Reality, The Journal of Physical Chemistry Letters, 6 (2015) 139-147.

[6] Y. Tachibana, L. Vayssieres, J.R. Durrant, Artificial photosynthesis for solar water-splitting, Nature Photonics, 6 (2012) 511-518.

[7] O. Zandi, T.W. Hamann, The potential versus current state of water splitting with hematite, Phys Chem Chem Phys, 17 (2015) 22485-22503.

[8] K. Sivula, F. Le Formal, M. Gratzel, Solar water splitting: progress using hematite (α-Fe$_2$O$_3$) photoelectrodes, ChemSusChem, 4 (2011) 432-449.

[9] A. Kay, I. Cesar, M. Gratzel, New benchmark for water photooxidation by nanostructured α-Fe$_2$O$_3$ films, Journal of the American Chemical Society, 128 (2006) 15714-15721.

[10] D.K. Bora, A. Braun, E.C. Constable, "In rust we trust". Hematite – the prospective inorganic backbone for artificial photosynthesis, Energy Environ. Sci., 6 (2013) 407-425.

[11] H. Dotan, K. Sivula, M. Gratzel, A. Rothschild, S.C. Warren, Probing the photoelectrochemical properties of hematite (α-Fe$_2$O$_3$) electrodes using hydrogen peroxide as a hole scavenger, Energy & Environmental Science, 4 (2011) 958-964.

[12] A. Murphy, P. Barnes, L. Randeniya, I. Plumb, I. Grey, M. Horne, J. Glasscock, Efficiency of solar water splitting using semiconductor electrodes, International Journal of Hydrogen Energy, 31 (2006) 1999-2017.

[13] J. Brillet, J.-H. Yum, M. Cornuz, T. Hisatomi, R. Solarska, J. Augustynski, M. Graetzel, K. Sivula, Highly efficient water splitting by a dual-absorber tandem cell, Nature Photonics, 6 (2012) 824-828.

[14] F. Le Formal, M. Grätzel, K. Sivula, Controlling Photoactivity in Ultrathin Hematite Films for Solar Water-Splitting, Advanced Functional Materials, 20 (2010) 1099-1107.

[15] K. Itoh, J.O.M. Bockris, Stacked thin-film photoelectrode using iron oxide, Journal of Applied Physics, 56 (1984) 874.

[16] J.H. Kennedy, K.W. Frese, Flatband Potentials and Donor Densities of Polycrystalline α - Fe$_2$O$_3$ Determined from Mott‐Schottky Plots, Journal of The Electrochemical Society, 125 (1978) 723-726.

[17] D.A. Wheeler, G. Wang, Y. Ling, Y. Li, J.Z. Zhang, Nanostructured hematite: synthesis, characterization, charge carrier dynamics, and photoelectrochemical properties, Energy & Environmental Science, 5 (2012) 6682.

[18] Y. Ling, G. Wang, D.A. Wheeler, J.Z. Zhang, Y. Li, Sn-Doped Hematite Nanostructures for Photoelectrochemical Water Splitting, Nano Letters, 11 (2011) 2119-2125.

[19] S.D. Tilley, M. Cornuz, K. Sivula, M. Grätzel, Light-Induced Water Splitting with Hematite: Improved Nanostructure and Iridium Oxide Catalysis, Angewandte Chemie International Edition, 49 (2010) 6405-6408.

[20] S.C. Warren, K. Voïtchovsky, H. Dotan, C.M. Leroy, M. Cornuz, F. Stellacci, C. Hébert, A. Rothschild, M. Grätzel, Identifying champion nanostructures for solar water-splitting, Nat Mater, 12 (2013) 842-849.

[21] M.E.A. Warwick, K. Kaunisto, D. Barreca, G. Carraro, A. Gasparotto, C. Maccato, E. Bontempi, C. Sada, T.-P. Ruoko, S. Turner, G. Van Tendeloo, Vapor Phase Processing of α-Fe2O3 Photoelectrodes for Water Splitting: An Insight into the Structure/Property Interplay, ACS Applied Materials & Interfaces, 7 (2015) 8667-8676.

[22] I. Tanyeli, L. Marot, M.C. van de Sanden, G. De Temmerman, Nanostructuring of iron surfaces by low-energy helium ions, ACS Appl Mater Interfaces, 6 (2014) 3462-3468.

[23] M. de Respinis, G. De Temmerman, I. Tanyeli, M.C. van de Sanden, R.P. Doerner, M.J. Baldwin, R. van de Krol, Efficient plasma route to nanostructure materials: case study on the use of m-WO$_3$ for solar water splitting, ACS Appl Mater Interfaces, 5 (2013) 7621-7625.

[24] A. Bieberle-Hütter, I. Tanyeli, R. Lavrijsen, B. Koopmans, R. Sinha, M.C.M. van de Sanden, Nanostructuring of iron thin films by high flux low energy helium plasma, Thin Solid Films, 631 (2017) 50-56.

[25] G.D. Temmerman, J.J. Zielinski, S.v. Diepen, L. Marot, M. Price, ELM simulation experiments on Pilot-PSI using simultaneous high flux plasma and transient heat/particle source, Nuclear Fusion, 51 (2011) 073008.

[26] P. Hiralal, H.E. Unalan, K.G. Wijayantha, A. Kursumovic, D. Jefferson, J.L. Macmanus-Driscoll, G.A. Amaratunga, Growth and process conditions of aligned and patternable films of iron(III) oxide nanowires by thermal oxidation of iron, Nanotechnology, 19 (2008) 455608.

[27] R.L. Tollman, E.A. Gulbransen, Crystal Morphology and Mechanisms of Growth of α ‐ Fe$_2$O$_3$ Whiskers on Iron, Journal of The Electrochemical Society, 114 (1967) 1227-1230.

[28] D.A. Voss, E.P. Butler, T.E. Mitchell, The Growth of Hematite Blades during the High Temperature Oxidation of Iron, Metallurgical Transactions A, 13 (1982) 929-935.

[29] L. Yuan, Y. Wang, R. Cai, Q. Jiang, J. Wang, B. Li, A. Sharma, G. Zhou, The origin of hematite nanowire growth during the thermal oxidation of iron, Materials Science and Engineering: B, 177 (2012) 327-336.

[30] I. Jogi, T.J. Jacobsson, M. Fondell, T. Watjen, J.O. Carlsson, M. Boman, T. Edvinsson, Phase Formation Behavior in Ultrathin Iron Oxide, Langmuir, 31 (2015) 12372-12381.

[31] A. Atkinson, Transport processes during the growth of oxide films at elevated temperature, Reviews of Modern Physics, 57 (1985) 437-470.

[32] W.M. Haynes, CRC Handbook of Chemistry and Physics, 97th Edition, CRC Press 2016.

[33] T. Lopes, L. Andrade, F. Le Formal, M. Gratzel, K. Sivula, A. Mendes, Hematite photoelectrodes for water splitting: evaluation of the role of film thickness by impedance spectroscopy, Phys Chem Chem Phys, 16 (2014) 16515-16523.

[34] J.A. Glasscock, P.R.F. Barnes, I.C. Plumb, N. Savvides, Enhancement of photoelectrochemical hydrogen production from hematite thin films by the introduction of Ti and Si, Journal of Physical Chemistry C, 111 (2007) 16477-16488.

[35] P. Hiralal, S. Saremi-Yarahmadi, B.C. Bayer, H. Wang, S. Hofmann, K.G. Upul Wijayantha, G.A.J. Amaratunga, Nanostructured hematite photoelectrochemical electrodes prepared by the low temperature thermal oxidation of iron, Solar Energy Materials and Solar Cells, 95 (2011) 1819-1825.

[36] L. Jia, K. Harbauer, P. Bogdanoff, I. Herrmann-Geppert, A. Ramírez, R. van de Krol, S. Fiechter, α-Fe$_2$O$_3$ films for photoelectrochemical water oxidation – insights of key performance parameters, J. Mater. Chem. A, 2 (2014) 20196-20202.

[37] L.M. Peter, K.G.U. Wijayantha, A.A. Tahir, Kinetics of light-driven oxygen evolution at α-Fe$_2$O$_3$electrodes, Faraday Discuss., 155 (2012) 309-322.

[38] G. Ketteler, W. Weiss, W. Ranke, R. Schlögl, Bulk and surface phases of iron oxides in an oxygen and water atmosphere at low pressure, Physical Chemistry Chemical Physics, 3 (2001) 1114-1122.

[39] D.L.A. de Faria, S. Venâncio Silva, M.T. de Oliveira, Raman microspectroscopy of some iron oxides and oxyhydroxides, J Raman Spectrosc, 28 (1997) 873-878.

[40] L. Stagi, J.A. De Toro, A. Ardu, C. Cannas, A. Casu, S.S. Lee, P.C. Ricci, Surface Effects Under Visible Irradiation and Heat Treatment on the Phase Stability of γ-Fe$_2$O$_3$ Nanoparticles and γ-Fe$_2$O$_3$−SiO$_2$ Core–Shell Nanostructures, The Journal of Physical Chemistry C, 118 (2014) 2857-2866.

[41] X. Zhang, Y. Niu, X. Meng, Y. Li, J. Zhao, Structural evolution and characteristics of the phase transformations between α-Fe$_2$O$_3$, Fe$_3$O$_4$ and γ-Fe$_2$O$_3$ nanoparticles under reducing and oxidizing atmospheres, CrystEngComm, 15 (2013) 8166.

[42] M. Rioult, D. Stanescu, E. Fonda, A. Barbier, H. Magnan, Oxygen Vacancies Engineering of Iron Oxides Films for Solar Water Splitting, Journal of Physical Chemistry C, 120 (2016) 7482-7490.

[43] T. Fujii, F.M.F. de Groot, G.A. Sawatzky, F.C. Voogt, T. Hibma, K. Okada, In situ XPS analysis of various iron oxide films grown by NO_2-assisted molecular-beam epitaxy, Physical Review B, 59 (1999) 3195-3202.

[44] A.P. Grosvenor, B.A. Kobe, M.C. Biesinger, N.S. McIntyre, Investigation of multiplet splitting of Fe 2p XPS spectra and bonding in iron compounds, Surface and Interface Analysis, 36 (2004) 1564-1574.

[45] Y. Hu, F. Boudoire, I. Hermann-Geppert, P. Bogdanoff, G. Tsekouras, B.S. Mun, G. Fortunato, M. Graetzel, A. Braun, Molecular Origin and Electrochemical Influence of Capacitive Surface States on Iron Oxide Photoanodes, The Journal of Physical Chemistry C, 120 (2016) 3250-3258.

[46] N.S. McIntyre, D.G. Zetaruk, X-ray photoelectron spectroscopic studies of iron oxides, Analytical Chemistry, 49 (1977) 1521-1529.

[47] C. Zhu, C. Li, M. Zheng, J.J. Delaunay, Plasma-Induced Oxygen Vacancies in Ultrathin Hematite Nanoflakes Promoting Photoelectrochemical Water Oxidation, ACS Appl Mater Interfaces, 7 (2015) 22355-22363.

[48] J.F. Moulder, W.F. Stickle, P.E. Sobol, K.D. Bomben, Handbook of X-ray photoelectron spectroscopy, Perkin-Elmer Corporation, Physical Electronics Division, Eden Prairie, Minnesota, 1992.

[49] A. Annamalai, A. Subramanian, U. Kang, H. Park, S.H. Choi, J.S. Jang, Activation of Hematite Photoanodes for Solar Water Splitting: Effect of FTO Deformation, The Journal of Physical Chemistry C, 119 (2015) 3810-3817.

[50] C.D. Bohn, A.K. Agrawal, E.C. Walter, M.D. Vaudin, A.A. Herzing, P.M. Haney, A.A. Talin, V.A. Szalai, Effect of Tin Doping on α-Fe_2O_3 Photoanodes for Water Splitting, The Journal of Physical Chemistry C, 116 (2012) 15290-15296.

[51] G. Ennas, A. Musinu, G. Piccaluga, D. Zedda, D. Gatteschi, C. Sangregorio, J.L. Stanger, G. Concas, G. Spano, Characterization of Iron Oxide Nanoparticles in an Fe_2O_3−SiO_2 Composite Prepared by a Sol−Gel Method, Chemistry of Materials, 10 (1998) 495-502.

[52] L. Machala, J.i. Tuček, R. Zbořil, Polymorphous Transformations of Nanometric Iron(III) Oxide: A Review, Chemistry of Materials, 23 (2011) 3255-3272.

[53] B. Klahr, S. Gimenez, F. Fabregat-Santiago, T. Hamann, J. Bisquert, Water oxidation at hematite photoelectrodes: the role of surface states, J Am Chem Soc, 134 (2012) 4294-4302.

[54] X. Shi, I. Herraiz-Cardona, L. Bertoluzzi, P. Lopez-Varo, J. Bisquert, J.H. Park, S. Gimenez, Understanding the synergistic effect of WO_3-$BiVO_4$ heterostructures by impedance spectroscopy, Phys Chem Chem Phys, 18 (2016) 9255-9261.

[55] G.J. Brug, A.L.G. van den Eeden, M. Sluyters-Rehbach, J.H. Sluyters, The analysis of electrode impedances complicated by the presence of a constant phase element, Journal of Electroanalytical Chemistry and Interfacial Electrochemistry, 176 (1984) 275-295.

[56] O. Zandi, T.W. Hamann, Determination of photoelectrochemical water oxidation intermediates on haematite electrode surfaces using operando infrared spectroscopy, Nat Chem, 8 (2016) 778-783.

[57] A. Lasia, Electrochemical Impedance Spectroscopy and its Applications, Springer, New York, 2014.

[58] M.P. Dare-Edwards, J.B. Goodenough, A. Hamnett, P.R. Trevellick, Electrochemistry and photoelectrochemistry of iron(III) oxide, Journal of the Chemical Society, Faraday Transactions 1: Physical Chemistry in Condensed Phases, 79 (1983) 2027-2041.

[59] H.K. Dunn, J.M. Feckl, A. Muller, D. Fattakhova-Rohlfing, S.G. Morehead, J. Roos, L.M. Peter, C. Scheu, T. Bein, Tin doping speeds up hole transfer during light-driven water oxidation at hematite photoanodes, Phys Chem Chem Phys, 16 (2014) 24610-24620.

[60] S. Kumari, C. Tripathi, A.P. Singh, D. Chauhan, R. Shrivastav, S. Dass, V.R. Satsangi, Characterization of Zn-doped hematite thin films for photoelectrochemical splitting of water, Curr. Sci., 91 (2006) 1062-1064.

[61] P.H. Borse, H. Jun, S.H. Choi, S.J. Hong, J.S. Lee, Phase and photoelectrochemical behavior of solution-processed Fe_2O_3 nanocrystals for oxidation of water under solar light, Applied Physics Letters, 93 (2008) 173103.

[62] S. Chandrasekaran, S.H. Hur, E.J. Kim, B. Rajagopalan, K.F. Babu, V. Senthilkumar, J.S. Chung, W.M. Choi, Y.S. Kim, Highly-ordered maghemite/reduced graphene oxide nanocomposites for high-performance photoelectrochemical water splitting, RSC Adv., 5 (2015) 29159-29166.

[63] R.R. Rangaraju, A. Panday, K.S. Raja, M. Misra, Nanostructured anodic iron oxide film as photoanode for water oxidation, Journal of Physics D: Applied Physics, 42 (2009) 135303.

[64] T. Sharifi, W.L. Kwong, H.-M. Berends, C. Larsen, J. Messinger, T. Wågberg, Maghemite nanorods anchored on a 3D nitrogen-doped carbon nanotubes substrate as scalable direct electrode for water oxidation, International Journal of Hydrogen Energy, 41 (2016) 69-78.
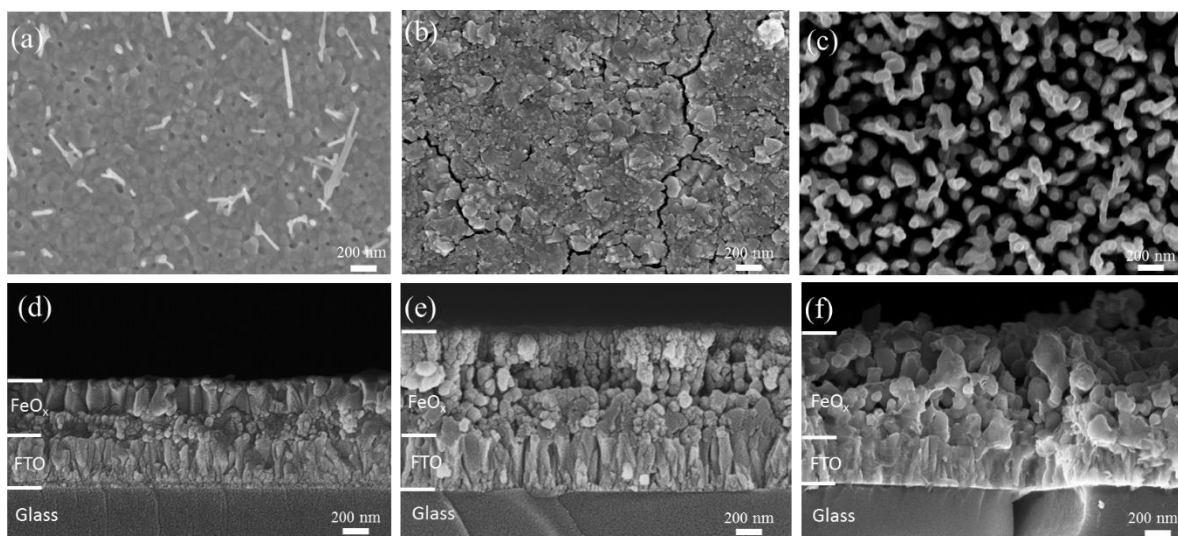
Figure 1 Top view and cross-section SEM images of (a, d) unexposed film (UE); (b, e) film exposed to plasma for 20 min (SE); and (c, f) film exposed to plasma for 50 min (LE). All images were taken after annealing (645°C for 10 min) and photoelectrochemical measurements in 1M NaOH.
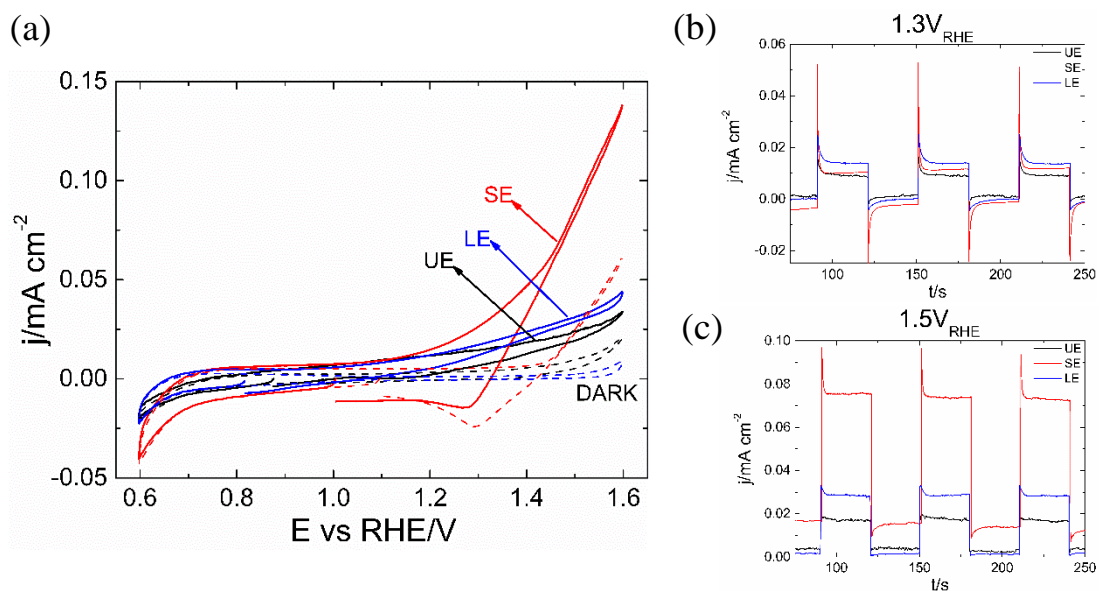
Figure 2. (a) Current-voltage J (V) characteristics in 1M NaOH in dark (dashed lines) and under illumination with light intensity of 80 mW cm^{-2} (solid lines) of UE (black) , SE (red) and LE (blue) thin films. (b) Chopped light chronoamperometric measurements at a potential of (b) 1.3 V_{RHE} and (c) 1.5 V_{RHE} (chopping rate = 0.033 s^{-1}).
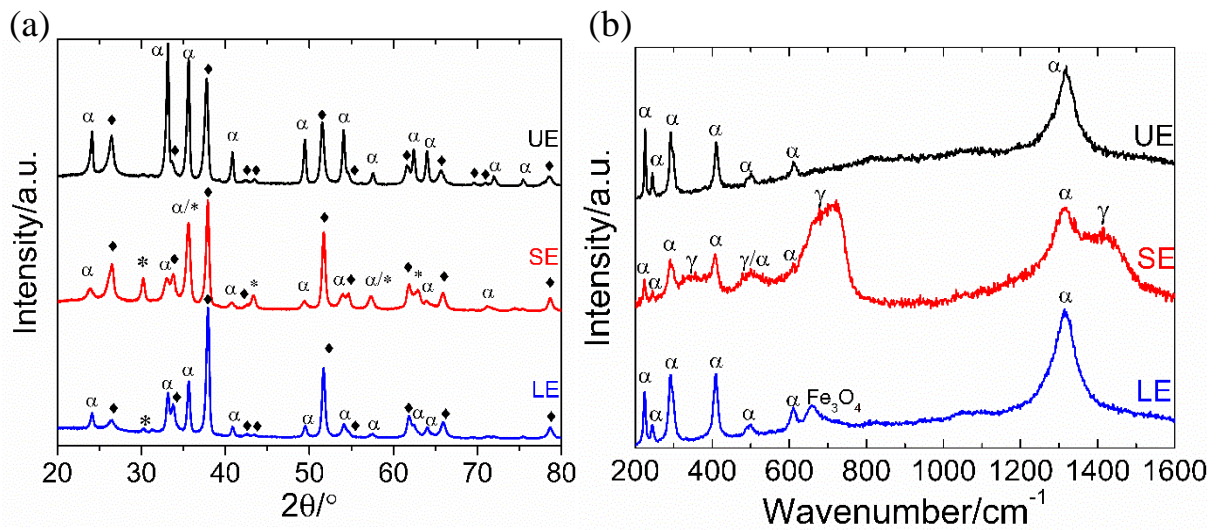
Figure 3 (a) XRD spectra and (b) Raman spectra of UE (black), SE (red) and LE (blue) thin films. All measurements were taken after annealing at 645°C for 10 min. For XRD spectra 'α' denotes peaks belonging to α-Fe_2O_3, '*' denotes peaks belonging to either γ-Fe_2O_3 or Fe_3O_4 and '♦' denotes peaks from FTO substrate; for Raman spectra 'α' denotes peaks assigned to α-Fe_2O_3, 'γ' denotes peaks assigned to γ-Fe_2O_3 and the namesake is used for the peak assigned to Fe_3O_4.
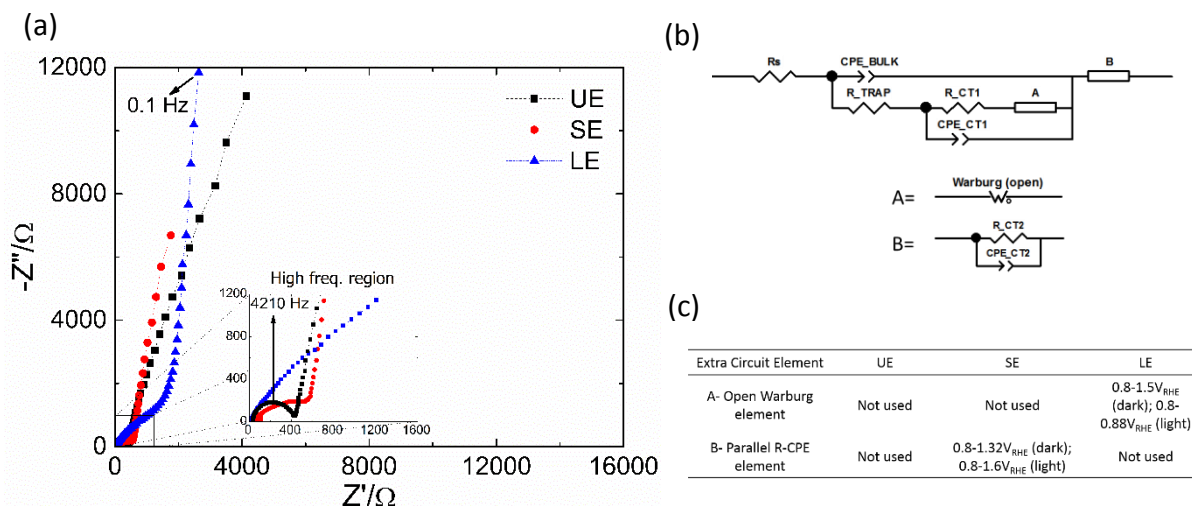
Figure 4. (a) Nyquist plots for EIS data measured in 1M NaOH under illumination of 80 mW cm^{-2} at an applied potential of 0.8 V$_{RHE}$. Inset in figure 4 (a) is a magnified plot of the impedance spectra in the high frequency region (represented by a square). The coloured symbols correspond to the different thin films: UE (■), SE (•) and LE (▲); (b) Equivalent circuit model (ECM) used for fitting of the EIS data; and (c) definition of the extra circuit elements A and B and attribution to samples, potential range, and illumination conditions.
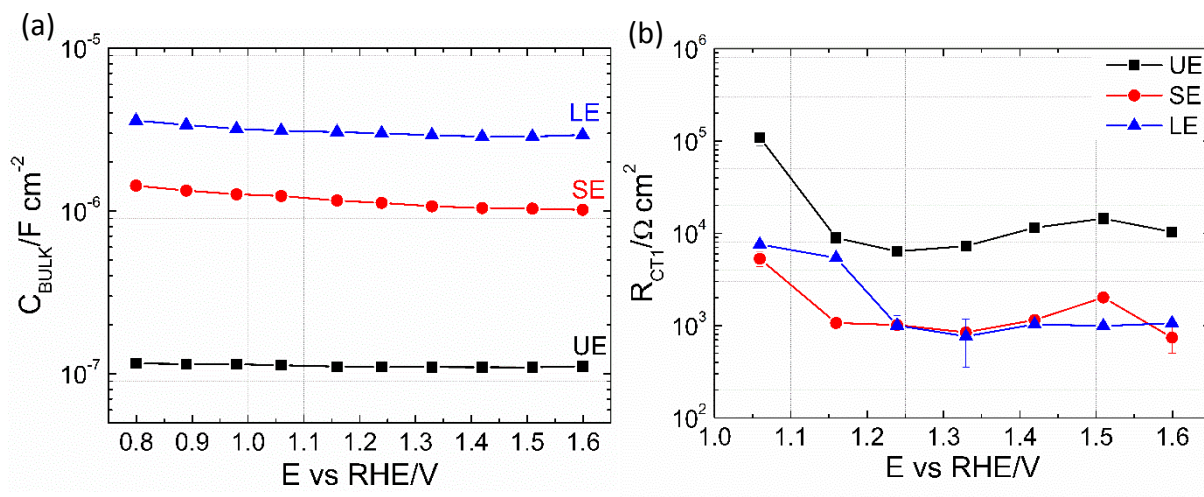
Figure 5 (a) Bulk capacitance (C_{BULK}) and (b) charge transfer resistance via hematite surface states (R_{CT1}) for all films plotted versus applied potential. The coloured symbols correspond to the different thin films: UE (■), SE (●) and LE (▲). The y-axis is plotted in logarithmic (base 10) units.
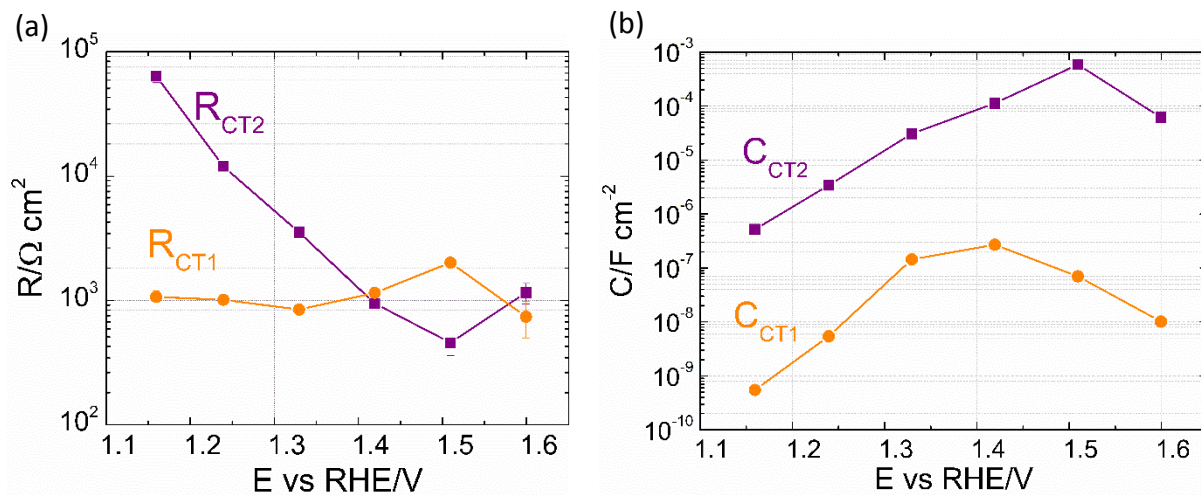
Figure 6 (a) Resistance and (b) capacitance for the SE thin film related to the 1st charge transfer process through hematite surface states (•) and the 2nd charge transfer process (■) plotted versus applied potential. The y-axis is plotted in logarithmic (base 10) units.